JOURNAL OF AIRCRAFT
Vol. 41, No. 6, November–December 2004

Modeling Viscous Transonic Limit-Cycle Oscillation Behavior Using a Harmonic Balance Approach

Jeffrey P. Thomas,* Earl H. Dowell,† and Kenneth C. Hall‡
Duke University, Durham, North Carolina 27708-0300

Presented is a harmonic-balance computational fluid dynamic approach for modeling limit-cycle oscillation behavior of aeroelastic airfoil configurations in a viscous transonic flow. For the NLR 7301 airfoil configuration studied, accounting for viscous effects is shown to significantly influence computed limit-cycle oscillation trends when compared to an inviscid analysis. A methodology for accounting for changes in mean angle of attack during limit-cycle oscillation is also developed.

Nomenclature

a	=	nondimensional location of airfoil elastic axis, e/b (Fig. 2)
b, c	=	semichord and chord, respectively
c_l, c_m	=	coefficient of lift and moment about elastic axis, respectively
$\bar{c}_{l_0}$, $\bar{c}_{m_0}$	=	zeroth harmonic or mean coefficient of lift and moment about elastic axis, respectively
$\bar{c}_{l_1}$, $\bar{c}_{m_1}$	=	first harmonic unsteady coefficient of lift and moment about elastic axis, respectively
D_h, D_α	=	airfoil plunge damping and torsional damping, respectively
e	=	location of airfoil elastic axis, measured positive aft of airfoil midchord
h, α	=	airfoil plunge and pitch coordinate degree of freedom, respectively
$\bar{h}_0$, $\bar{\alpha}_0$	=	zeroth harmonic or mean airfoil plunge and pitch amplitude, respectively
$\bar{h}_1$, $\bar{\alpha}_1$	=	first harmonic unsteady airfoil plunge and pitch amplitude, respectively
I_α	=	second moment of inertia of airfoil about elastic axis
j	=	$\sqrt{-1}$
K_h, K_α	=	airfoil plunge stiffness and torsional stiffness about elastic axis, respectively
M_∞	=	freestream Mach number
m	=	wind-tunnel experimental wing mass
m_h	=	wind-tunnel plunge coordinate total mass, $m + m_{\mathrm{SD}} + m_{\mathrm{SP}}$
m_{SD}	=	wind-tunnel shift device mass
m_{SP}	=	wind-tunnel suspension device mass
N_H	=	number of harmonics used in harmonic balance computational fluid dynamics flow solver method
Re, Im	=	real and imaginary part, respectively
Re_∞	=	freestream Reynolds number
r_α	=	radius of gyration of airfoil about elastic axis, $r_\alpha^2 = I_\alpha/mb^2$
S_α	=	first moment of inertia of airfoil about elastic axis
s	=	wind-tunnel experimental model span
T	=	period, time for one cycle of oscillation
U_∞	=	freestream velocity
V	=	reduced velocity, $U_\infty/\sqrt{(\mu)\omega_\alpha b}$
x_α	=	airfoil static unbalance, S_α/mb
y	=	dimensional distance normal to the airfoil surface
y^+	=	nondimensional distance normal to the airfoil surface, $y\sqrt{(\tau_w/\rho)}/\nu$
ζ_h	=	plunge coordinate damping coefficient, $D_h/2m\omega_h$
ζ_α	=	pitch coordinate damping coefficient, $D_\alpha/2I_\alpha\omega_\alpha$
μ	=	mass ratio, $m/\pi\rho_\infty b^2 s$
ν	=	kinematic viscosity
ρ, ρ_∞	=	local and freestream density, respectively
τ_w	=	airfoil surface tangential shear stress
ω, $\bar{\omega}$	=	frequency and reduced frequency based on airfoil chord, $\omega c/U_\infty$, respectively
ω_h	=	plunge coordinate natural frequency based on wing mass, $\sqrt{(K_h/m)}$
ω_α	=	pitch coordinate natural frequency, $\sqrt{(K_\alpha/I_\alpha)}$

Subscript

f	=	flutter point condition

Received 5 September 2002; revision received 5 April 2004; accepted for publication 1 April 2004.

*Research Assistant Professor, Department of Mechanical Engineering and Materials Science. Member AIAA.
†J. A. Jones Professor, Department of Mechanical Engineering and Materials Science, and Dean Emeritus, School of Engineering. Fellow AIAA.
‡Professor and Department Chairperson, Department of Mechanical Engineering and Materials Science. Associate Fellow AIAA.

Introduction

A NOVEL approach for modeling limit-cycle oscillation (LCO) behavior of aeroelastic airfoil configurations in viscous transonic flows is presented. The method is based on a harmonic balance (HB) flow solver technique for efficiently modeling nonlinear unsteady aerodynamics.[1,2] The primary objective of the current study is to assess the capability of the HB/LCO solution methodology to model transonic viscous flow phenomena such as shock-induced boundary-layer separation, and to determine if such effects have an influence on LCO behavior. Recent two-dimensional experimental LCO investigations by Schewe and Deyhle,[3] Schewe et al.,[4] and Knipfer and Schewe[5] have also motivated the present research. In addition to viscous effects, and unlike the NACA 64A010 airfoil configuration studied by Thomas et al.,[2] we now also consider nonsymmetric airfoil sections at nonzero angles of attack. As will be shown in the following, this requires the solution of one additional equation for the mean, that is, zeroth harmonic, angle of attack of the LCO.

The primary motivation for the development of the HB/LCO solution methodology has been to construct an efficient computational procedure for modeling LCO behavior. Figure 1a illustrates a typical flutter onset boundary in the reduced velocity vs Mach number plane, including the commonly observed "flutter speed dip." As one moves from point A, a reduced velocity below the flutter onset condition, to point B, a reduced velocity above the flutter onset condition, LCO may be encountered. Figure 1b illustrates three possible types of LCO behavior one might observe.

Curve 1 represents a stable LCO behavior with no LCO occurring below the linear flutter speed. This type of LCO behavior is

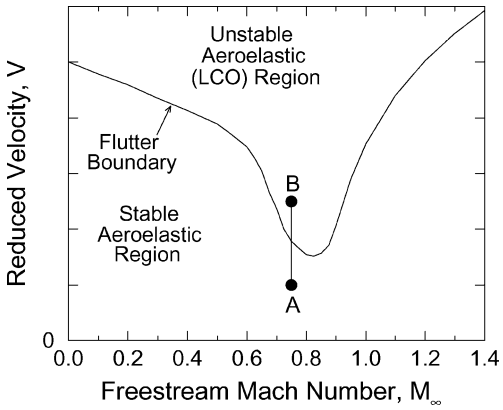

a) Mach number flutter speed dip trend

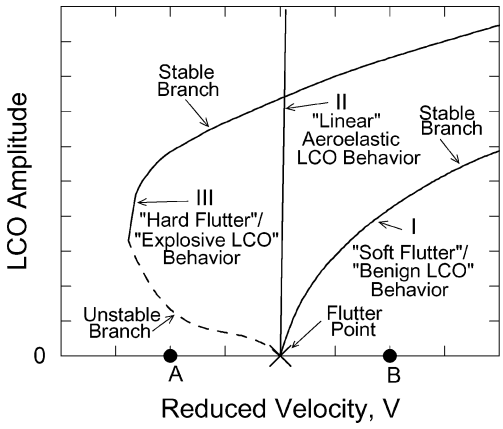

b) LCO behavior trends near flutter onset condition

Fig. 1 Example of LCO behavior trends.

also sometimes referred to as soft flutter, or benign LCO, per se, in that the nonlinear effects help to reduce the amplitude of the oscillations. Of course, structural failure may eventually be an issue if the amplitude of the LCO becomes too large. For the type of LCO behavior illustrated by curve 2, as soon as one reaches the flutter onset condition, any further increase in reduced velocity immediately results in very large LCO motion. Finally, curve 3 illustrates unstable LCO behavior. A configuration exhibiting this very dangerous type of LCO trend is susceptible to explosive LCO, whereby a disturbance of sufficient magnitude may be capable of triggering LCO at reduced velocities even below the flutter onset condition. As will be shown, the HB/LCO solution methodology is a computationally efficient technique for determining such LCO trends.

Theoretical Development

Fluid Dynamic Model

For the model configuration studied in this investigation, we consider both viscous and inviscid fluid dynamic models. The HB flow solver technique provides an efficient method with which to model nonlinear unsteady aerodynamic effects for finite amplitude motions of a prescribed frequency.

As is discussed by Hall et al.[1] and Thomas et al.,[2] the HB method is implemented within the framework of a conventional computational fluid dynamics (CFD) solver. The vector of unsteady flow conservation variables $\boldsymbol{U}(\boldsymbol{x}_i, t)$ at each computational mesh point $\boldsymbol{x}_i$ is approximated in a truncated Fourier expansion as

$$\boldsymbol{U}(\boldsymbol{x}_i, t) \approx \sum_{n=-N_H}^{N_H} \hat{\boldsymbol{U}}_n(\boldsymbol{x}_i) e^{jn\omega t} \tag{1}$$

where $\hat{\boldsymbol{U}}_n(\boldsymbol{x}_i)$ is the nth harmonic coefficient, and N_H is number of harmonics used in the expansion. McMullen et al.[6,7] are also investigating a similar expansion technique for unsteady Euler and Navier–Stokes flows.

Normally, the HB development proceeds by first substitution of Eq. (1) into the governing flow equations. One then subsequently goes through the process of balancing all of the resulting terms proportional to $e^{jn\omega t}$ for each n $(-N_H \le n \le N_H)$. This, in turn, yields $2N_H + 1$ equations for the $2N_H + 1$ harmonic coefficients $\hat{\boldsymbol{U}}_n$. This straightforward approach to the HB formulation is, however, typically difficult to implement for complex systems of equations such as those arising from Euler and Navier–Stokes flows.

Hall et al.,[1] however, recently devised an alternative approach to the HB derivation, whereby the method is formulated in terms of time-domain variables. That is, instead of working in terms of the Fourier coefficient variables $\hat{\boldsymbol{U}}_n(\boldsymbol{x}_i)$, one instead considers, as dependent variables, flow solutions stored at $2N_H+1$ equally spaced subtime levels $[\boldsymbol{U}(\boldsymbol{x}_i, t_n)]$ over the period of one cycle of motion. The Fourier and time-domain variables are, in fact, related to one another via a constant Fourier transformation matrix.

Working in terms of subtime level variables circumvents the necessity of having to go though the balancing step of the HB method, and, in fact, it allows one to easily formulate the HB technique within the framework of an existing steady CFD solver. (See Hall et al.[1] and Thomas et al.[2] for further details.) For the results presented here, the CFD method is a variant of standard Lax–Wendroff scheme(see Refs. 8 and 9) in conjunction with the one-equation turbulence model of Spalart and Allmaras.[10]

Two-Dimensional Airfoil Aeroelastic Model

The frequency domain form of the unsteady aeroelastic equations governing the typical pitch/plunge airfoil configuration (Fig. 2) can be written as

$$\boldsymbol{G}\boldsymbol{u} = (V^2/\pi)\boldsymbol{f} \tag{2}$$

where

$$\boldsymbol{G} = -(\mu/4)\bar{\omega}^2 V^2 \boldsymbol{M} + j\sqrt{\mu}\bar{\omega} V \boldsymbol{D} + \boldsymbol{K} \tag{3}$$

$$\boldsymbol{M} = \begin{bmatrix} m_h/m & x_\alpha \\ x_\alpha & r_\alpha^2 \end{bmatrix}, \qquad \boldsymbol{D} = \begin{bmatrix} \zeta_h(\omega_h/\omega_\alpha) & 0 \\ 0 & \zeta_\alpha r_\alpha^2 \end{bmatrix}$$

$$\boldsymbol{K} = \begin{bmatrix} (\omega_h/\omega_\alpha)^2 & 0 \\ 0 & r_\alpha^2 \end{bmatrix}, \qquad \boldsymbol{u} = \begin{Bmatrix} \bar{h}_1/b \\ \bar{\alpha}_1 \end{Bmatrix}, \qquad \boldsymbol{f} = \begin{Bmatrix} -\bar{c}_{l_1} \\ 2\bar{c}_{m_1} \end{Bmatrix} \tag{4}$$

Static Aeroelastic Equation

For the present investigation, because nonsymmetric airfoil sections and/or nonzero angles of attack are being considered, one must also include the effects of changes in the computed mean flow, for example, zeroth harmonic, for different LCO amplitudes, which, in turn, effect the mean angle of attack $\bar{\alpha}_0$ of the LCO. This requires

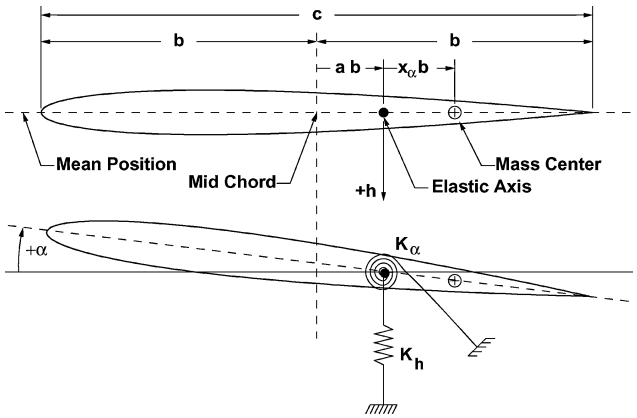

Fig. 2 Geometry for typical (pitch/plunge) two-degree-of-freedom airfoil section aeroelastic model.

that one must also satisfy the static, for example, zeroth harmonic, aeroelastic equation for the pitch degree of freedom

$$K_\alpha\left(\bar{\alpha}_0 - \alpha_{e_0}\right) = q_\infty c^2 s \bar{c}_{m_0}(\bar{\omega}, \bar{\alpha}_0, \bar{\alpha}_1, \bar{h}_1/b) \tag{5}$$

where α_{e_0} is the angle of attack for zero spring stiffness in the pitch coordinate. After some rearrangement, this equation can be written as

$$\bar{\alpha}_0 = \alpha_{e_0} + \left(2V^2/\pi r_\alpha^2\right)\bar{c}_{m_0} \tag{6}$$

The static aeroelastic equation for the plunge coordinate $\bar{h}_0$ establishes the vertical position of the airfoil. This equation is decoupled from both the static pitch equation and the first harmonic unsteady aeroelastic equations (Eq. 2) and, thus, is neglected in the following theoretical development.

LCO Solution Procedure

In the following, we describe the technique in which the HB method can be used for modeling LCOs. The methodology was initially developed and presented by Thomas et al.[2] The HB/LCO solution procedure starts by rewriting Eq. (2) as

$$\boldsymbol{G}\boldsymbol{v} = \left(V^2/\pi\bar{\alpha}_1\right)\boldsymbol{f} \tag{7}$$

where

$$\boldsymbol{v} = \begin{Bmatrix} \bar{h}_1/\bar{\alpha}_1 b \\ 1 \end{Bmatrix} \tag{8}$$

In this form, Eq. (2) has been divided through by the first harmonic unsteady pitch amplitude $\bar{\alpha}_1$. This enables one to consider $\bar{\alpha}_1$ as the independent variable in the HB/LCO solution process.

Defining $\boldsymbol{R}(\boldsymbol{L})$ as the vector operator representing residual of Eq. (6), together with the residual of the real and imaginary parts of Eq. (7), one may write the governing steady and unsteady aeroelastic equations in vector form as

$$\boldsymbol{R}(\boldsymbol{L}) = \begin{Bmatrix} \bar{\alpha}_0 - \alpha_{e_0} - \dfrac{2V^2}{\pi r_\alpha^2}\bar{c}_{m_0} \\ \tilde{\boldsymbol{G}}\tilde{\boldsymbol{v}} - \dfrac{V^2}{\pi\bar{\alpha}_1}\tilde{\boldsymbol{f}} \end{Bmatrix} = \boldsymbol{0} \tag{9}$$

where $\tilde{\boldsymbol{G}}$ is the 4×4 matrix

$$\tilde{\boldsymbol{G}} = \begin{bmatrix} \boldsymbol{G}_{\mathrm{Re}} & -\boldsymbol{G}_{\mathrm{Im}} \\ \boldsymbol{G}_{\mathrm{Im}} & \boldsymbol{G}_{\mathrm{Re}} \end{bmatrix} \tag{10}$$

$\tilde{\boldsymbol{v}}$ and $\tilde{\boldsymbol{f}}$ are

$$\tilde{\boldsymbol{v}} = \begin{Bmatrix} \mathrm{Re}(\bar{h}_1/\bar{\alpha}_1 b) \\ 1 \\ \mathrm{Im}(\bar{h}_1/\bar{\alpha}_1 b) \\ 0 \end{Bmatrix}, \qquad \tilde{\boldsymbol{f}} = \begin{Bmatrix} -\mathrm{Re}\left(\bar{c}_{l_1}\right) \\ 2\,\mathrm{Re}\left(\bar{c}_{m_1}\right) \\ -\mathrm{Im}\left(\bar{c}_{l_1}\right) \\ 2\,\mathrm{Im}\left(\bar{c}_{m_1}\right) \end{Bmatrix} \tag{11}$$

and $\boldsymbol{L}$ is the vector of unknown LCO variables

$$\boldsymbol{L} = \begin{Bmatrix} \bar{\alpha}_0 \\ V \\ \bar{\omega} \\ \mathrm{Re}(\bar{h}_1/\bar{\alpha}_1 b) \\ \mathrm{Im}(\bar{h}_1/\bar{\alpha}_1 b) \end{Bmatrix} \tag{12}$$

We have found that a Newton–Raphson nonlinear root finding technique is an efficient and stable method for quickly solving for a root $\boldsymbol{L}$ of Eq. (9). That is, for a specified unsteady pitch amplitude $\bar{\alpha}_1$, one can implement an iterative process whereby the $(n+1)$th update to the LCO solution $\boldsymbol{L}$ is given by

$$\boldsymbol{L}^{n+1} = \boldsymbol{L}^n - \left[\frac{\partial \boldsymbol{R}(\boldsymbol{L}^n)}{\partial \boldsymbol{L}}\right]^{-1}\boldsymbol{R}(\boldsymbol{L}^n) \tag{13}$$

where

$$\left[\frac{\partial \boldsymbol{R}(\boldsymbol{L})}{\partial \boldsymbol{L}}\right] = \begin{bmatrix} | & | & | & | & | \\ \dfrac{\partial \boldsymbol{R}}{\partial \bar{\alpha}_0} & \dfrac{\partial \boldsymbol{R}}{\partial V} & \dfrac{\partial \boldsymbol{R}}{\partial \bar{\omega}} & \dfrac{\partial \boldsymbol{R}}{\partial \mathrm{Re}(\bar{h}_1/\bar{\alpha}_1 b)} & \dfrac{\partial \boldsymbol{R}}{\partial \mathrm{Im}(\bar{h}_1/\bar{\alpha}_1 b)} \\ | & | & | & | & | \end{bmatrix} \tag{14}$$

We have also found that one can get very good convergence by simply approximating the column vectors of $\partial \boldsymbol{R}(\boldsymbol{L}^n)/\partial \boldsymbol{L}$ using forward differencing. That is,

$$\frac{\partial \boldsymbol{R}(\boldsymbol{L}^n)}{\partial \bar{\alpha}_0} \approx \frac{\boldsymbol{R}\left(\boldsymbol{L}^n, \bar{\alpha}_0^n + \epsilon\right) - \boldsymbol{R}\left(\boldsymbol{L}^n, \bar{\alpha}_0^n\right)}{\epsilon} \tag{15}$$

$$\frac{\partial \boldsymbol{R}(\boldsymbol{L}^n)}{\partial V} \approx \frac{\boldsymbol{R}(\boldsymbol{L}^n, V^n + \epsilon) - \boldsymbol{R}(\boldsymbol{L}^n, V^n)}{\epsilon} \tag{16}$$

etc., for a small ϵ.

For each step of the LCO solution procedure, the HB flow solver is implemented by the use of the current LCO frequency $\bar{\omega}$ and structural mode shape $(\bar{h}_1/\bar{\alpha}_1 b)$, for the prescribed LCO pitch amplitude $\bar{\alpha}_1$, to provide an update for the LCO aerodynamic loading, that is, $\bar{c}_{l_1}$, $\bar{c}_{m_0}$, and $\bar{c}_{m_1}$. The technique is marched until a suitable level of convergence is achieved, and the linear flutter solution has been found to provide an excellent starting solution for the iterative process. Typically, only a few iterations are required to achieve convergence.

Steady and Unsteady Aerodynamic Modeling of the NLR 7301 Airfoil

The model configuration under consideration is the NLR 7301 constant airfoil section wing tested extensively by Schewe and Deyhle,[3] Schewe et al.,[4] and Knipfer and Schewe.[5] Transonic two-degree-of-freedom aeroelastic experimental studies were conducted for various Mach numbers and angles of attack, and, in some instances, LCO was observed.

The experimental condition we model using the HB/LCO solution methodology is referred to by Schewe et al.[4] as measured point condition MP77. This is an LCO condition where the wind-tunnel test section Mach number, mean angle of attack, and Reynolds number are reported to be[4,5] $M_\infty = 0.768$, $\bar{\alpha}_0 = 1.28$ deg, and $Re_\infty = 1.727 \times 10^6$, respectively. The experimental model[3–5] consists of a 1-m span $(s = 1.0m)$ by 0.3-m chord $(c = 0.3m)$ NLR 7301 constant airfoil section wing placed in a 1-m by 1-m cross section wind-tunnel test section. The elastic axis of the model is positioned at the wing quarter-chord. Because of the relatively large size of the model in relation to the wind-tunnel cross section, wind-tunnel interference effects are known to be significant.

The harmonic balance based CFD flow solver used in the present investigation is capable of only modeling isolated airfoil sections in an unbounded freestream. As such, a method of accounting for wind-tunnel wall interference effects is necessary. Unfortunately, simple classical analytical wind-tunnel wall interference correction methods have the tendency to breakdown for transonic Mach numbers. As such, one method to account for wind-tunnel wall interference effects is to seek out a combination of Mach number and angle of attack for the CFD method such that the computed surface pressure distribution matches as best as possible the experimental distribution. Investigators such as Weber et al.[11] and Tang et al.,[12] who are also studying computational techniques for modeling test condition MP77, have recently reported, however, that such a combination of corrected Mach number and angle of attack has been quite elusive to determine and appears perhaps not to exist. In fact, Castro et al.[13,14] have recently taken the approach of adding appropriate

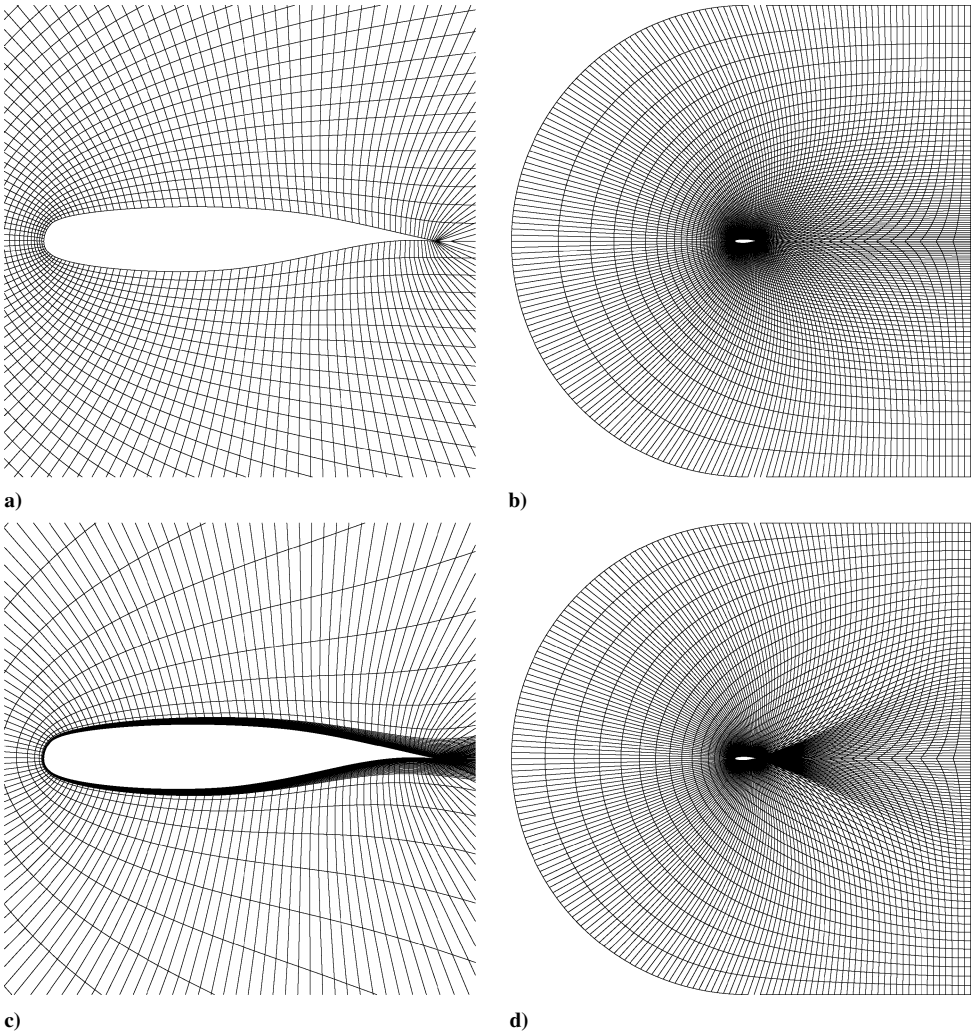

Fig. 3 Computational grids used for the NLR 7301 airfoil configuration: a) inviscid mesh close-up, b) inviscid mesh overall, c) viscous mesh close-up, and d) viscous mesh overall.

boundary conditions to their CFD flow solver to account for the wind-tunnel walls. However, Castro et al.[13,14] have noted that there is still much difficulty in correctly accounting for wind-tunnel wall porosity effects.

Rather than go through a similar and time-consuming exercise of trying to determine a combination of corrected Mach number and angle of attack in an effort to precisely match the experimental surface pressure distribution, we have decided as a first approximation to proceed by fixing the Mach number to $M_\infty = 0.75$ and to then simply adjust the angle of attack until the computed CFD solution steady flow lift matches the experimental lift.

Computational Mesh

Figure 3 shows sample inviscid and viscous computational grids used by the HB CFD solver for the NLR 7301 airfoil configuration. A C-grid structured mesh topology is used. The medium mesh viscous grid shown in Figs. 3c and 3d consists of 49 mesh points radially and 193 mesh points circumferentially, with a total of 145 mesh points surrounding the airfoil surface, and the remainder of the circumferential mesh points being distributed in the wake. For all grids, the outer boundary extends to a distance of 10 chord lengths from the center of the airfoil. Similar 385×97 and 97×25 viscous meshes have also been created. (See Mesh and Harmonic Convergence Issues section for more details.) Figures 3a and 3b show an inviscid 193×49 mesh.

For the viscous flow simulations, the grid spacing has been placed close enough to the airfoil surface such that the maximum computed value for the nondimensional distance to the wall spacing parameter y^+ is approximately five for the 193×49 viscous mesh.

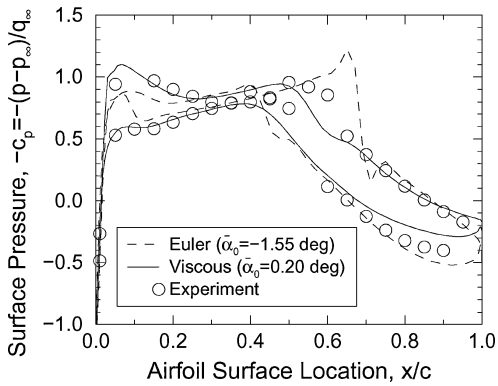

Fig. 4 Computed steady flow surface pressure distributions: NLR 7301 airfoil section, $M_\infty = 0.75$, and $Re_\infty = 1.727 \times 10^6$.

Steady Flow Simulations

With the Mach number set to $M_\infty = 0.75$, steady flows are computed by simply running the HB flow solver with zero harmonics. To match the experimentally observed lift coefficient of $\bar{c}_{l_0} = 0.27$, an angle of attack of $\bar{\alpha}_0 = 0.2$ deg is needed for the viscous flow model, whereas an angle of attack of $\bar{\alpha}_0 = -1.55$ deg is required for the inviscid model.

For both the inviscid and viscous flow models, Fig. 4 shows the computed and experimental steady surface pressure distributions, whereas Fig. 5 shows computed steady Mach contours. In this instance, the 193×49 viscous and inviscid grids have been used. A strong shock is readily apparent for the inviscid model.

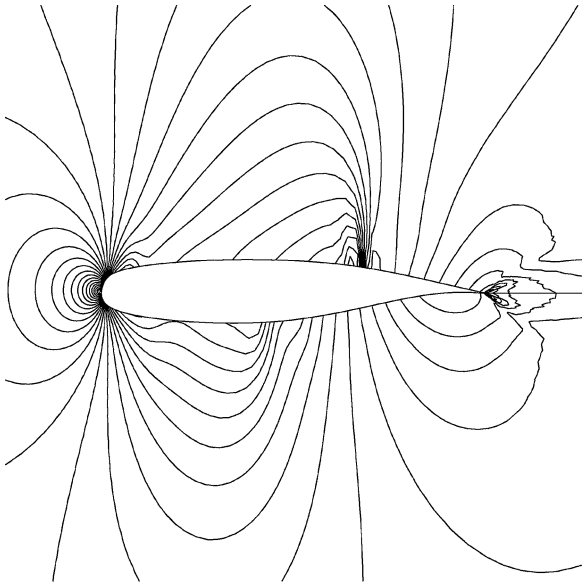

a) Inviscid

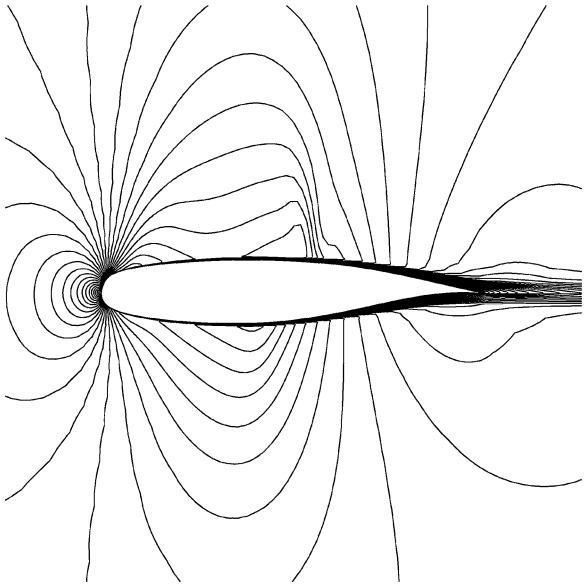

b) Viscous

Fig. 5 Computed steady flow mach number contours: NLR 7301 airfoil section, $M_\infty = 0.75$, and $Re_\infty = 1.727 \times 10^6$.

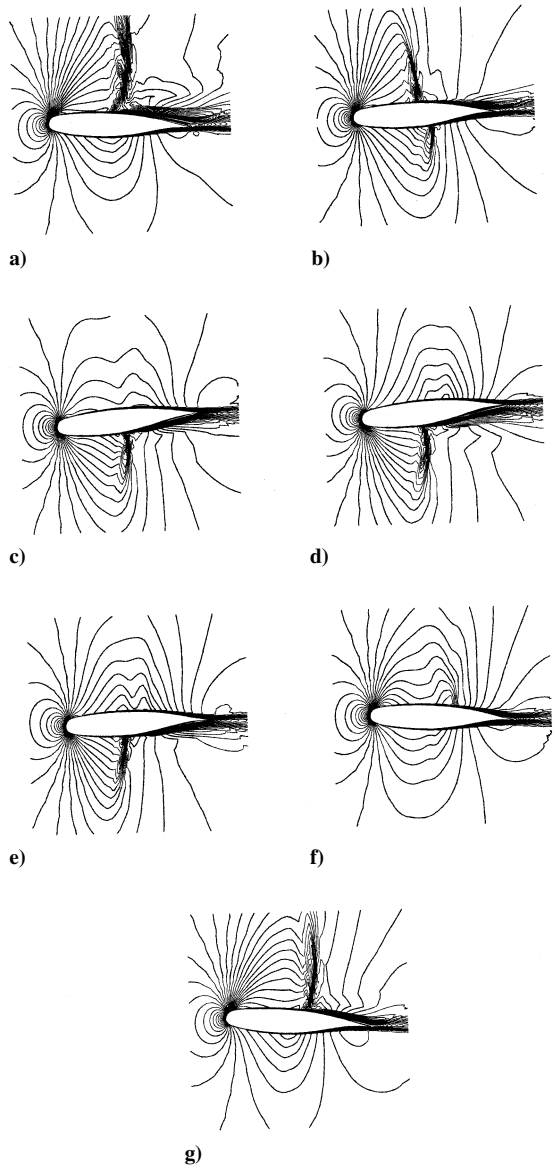

a) b) c) d) e) f) g)

Fig. 6 Computed HB method unsteady Mach number contours: NLR 7301 airfoil section: $M_\infty = 0.75$, $Re_\infty = 1.727 \times 10^6$, $\bar{\alpha}_0 = 0.2$ deg, $\bar{\alpha}_1 = 5$ deg, $\bar{\omega} = 0.3$, $a = -0.5$, and $N_H = 3$ [$\Delta T = T/(2N_H + 1) = T/7$]: a) t_0, b) $t_0 + \Delta T$, c) $t_0 + 2\Delta T$, d) $t_0 + 3\Delta T$, e) $t_0 + 4\Delta T$, f) $t_0 + 5\Delta T$, and g) $t_0 + 6\Delta T$.

Unsteady Flow Simulations

Next, Fig. 6 shows computed Mach contours during one cycle of motion for the fine mesh (193 × 49) viscous flow CFD model of the NLR 7301 airfoil when oscillating about the quarter-chord at a pitch amplitude of $\bar{\alpha}_1 = 5$ deg and a reduced frequency $\bar{\omega} = 0.3$. Clearly evident is shock-induced boundary-layer separation over both the upper and lower surfaces during a cycle of motion.

Mesh and Harmonic Convergence Issues

To have confidence in the accuracy of the LCO solutions that will be discussed in the following sections, one needs to determine whether or not a sufficient level of grid resolution is being used to model the correct flow physics accurately. For the harmonic balance solver, the issue of solution resolution is further complicated by the fact that one must also consider harmonic convergence. That is, whether or not a sufficient number of harmonic expansion terms N_H are being used in the HB flow solver. Thus, much like when working with time-domain methods where one must also be concerned with temporal accuracy in addition to spatial accuracy, for the HB method, both mesh and harmonic resolution must be considered.

To demonstrate sufficient mesh and harmonic convergence for the current NLR 7301 aeroelastic configuration, we consider a case where the airfoil is pitching about the quarter-chord for the largest pitch amplitude investigated in this study, which, in this instance, is $\bar{\alpha}_1 = 5$ deg. This will be discussed further in the LCO results section. The unsteady reduced frequency is chosen to be $\bar{\omega} = 0.3$, which is near the reduced frequency of the experimentally observed LCO.

First, we consider mesh resolution effects when three harmonics are used for the HB method. Shown in Fig. 7 are the computed zeroth harmonic (Fig. 7a), and real (Fig. 7b) and imaginary (Fig. 7c) first harmonic unsteady airfoil surface pressure distributions for three different grid resolutions. Namely, 97 × 25, 193 × 49, and 385 × 97 meshes. The 193 × 49 mesh is created from the 193 × 49 mesh by removal of every other mesh point, and, likewise, the 97 × 25 mesh is created from the 193 × 49 mesh by removal of every other mesh point. As can be seen, the pressure distributions are very similar for all three mesh resolutions. Even for the imaginary part of the unsteady pressure, where, for the midsection of the airfoil there are some more noticeable differences between the three different mesh resolutions, it can be seen that the results are converging as mesh resolution increases.

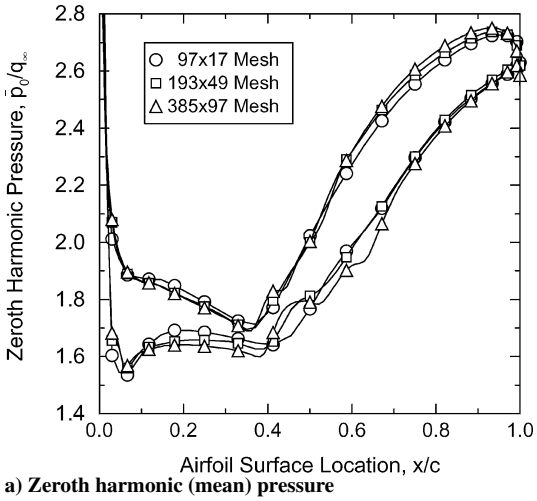

a) Zeroth harmonic (mean) pressure

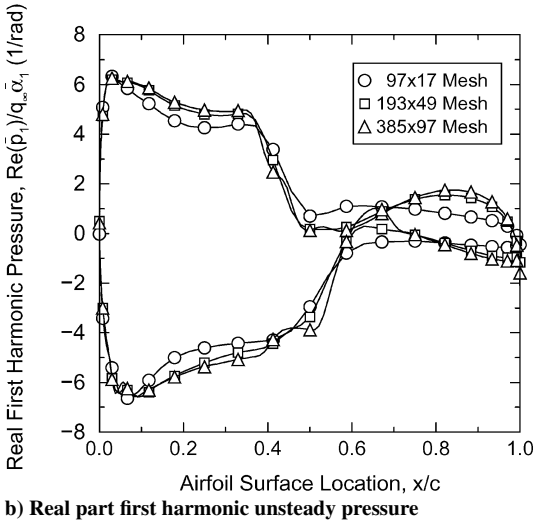

b) Real part first harmonic unsteady pressure

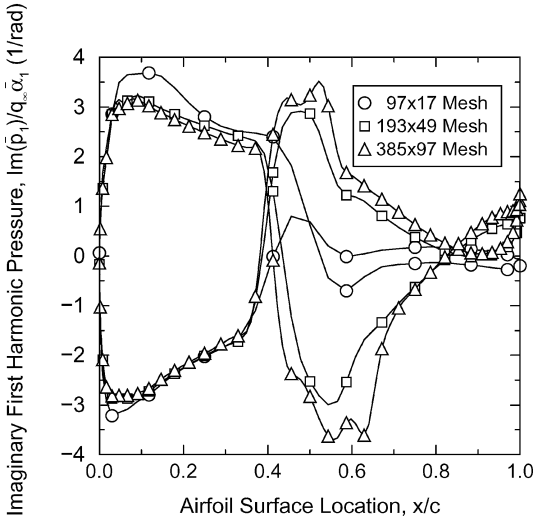

c) Imaginary part first harmonic unsteady pressure

Fig. 7 Mesh resolutions trends for computed steady and unsteady surface pressure distributions when using three harmonics in HB method, $N_H = 3$.

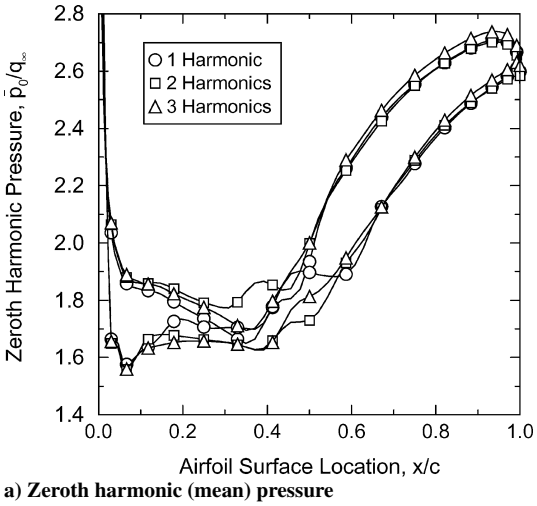

a) Zeroth harmonic (mean) pressure

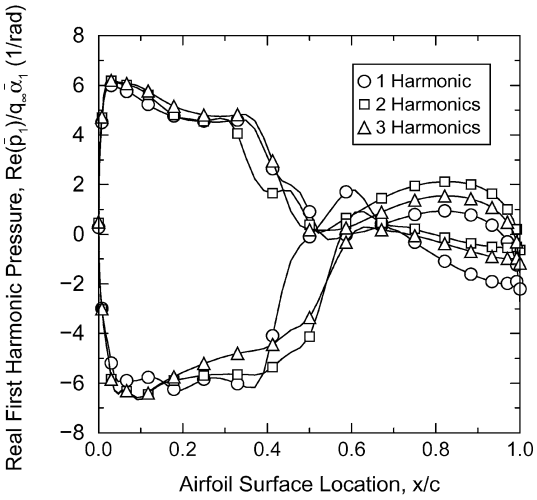

b) Real part zeroth harmonic unsteady pressure

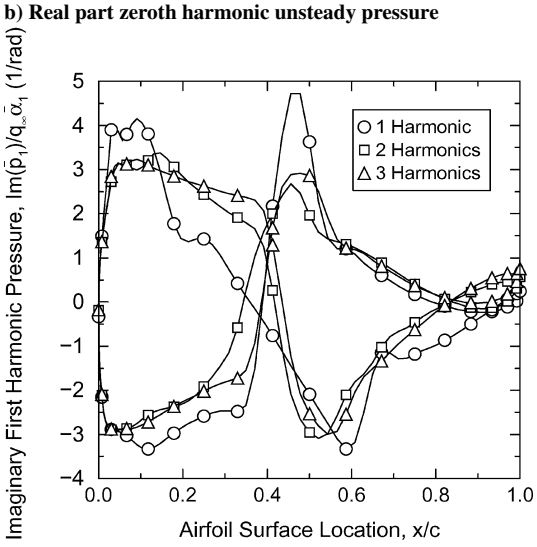

c) Imaginary part zeroth harmonic unsteady pressure

Fig. 8 Number of harmonics used in HB method solution trends for steady and unsteady surface pressure distributions when using 193 × 49 mesh.

Because of the four to eight times increase in computational cost for the Lax–Wendroff method when doubling mesh resolution in two dimensions (and we stress that this has nothing to do with the HB technique), we have chosen to proceed with the 193×49 mesh. The reason for the four to eight times computational cost increase is simply because, when doubling mesh resolution in each computational coordinate on a structured mesh, the new mesh will have four times as many nodes and, thus, four times as many computations. Furthermore, because of the smaller grid spacing on the finer mesh, for the Lax–Wendroff method, the maximum allowable iteration step size decreases, which typically means that more iterations are required to achieve solution convergence.

Next, Fig. 8 shows the harmonic convergence trend on the 193×49 mesh. Shown again are the computed zeroth and first harmonic airfoil surface pressure distributions for three different numbers of harmonics used in the HB method. Namely $N_H = 1, 2,$

and 3. The results look fairly well converged, even with just two harmonics. The computational cost of the HB method grows at a rate of $2 \times N_H + 1$ times the cost of a steady flow computation. We have chosen to proceed with two harmonics for the remaining analysis in this paper.

LCO Modeling for the NLR 7301 Configuration

Structural Parameters

The structural parameters used for the LCO analysis are those presented by Knipfer and Schewe[5] and Schewe et al.[4] Table 1 summarizes values for dimensional and nondimensional quantities.

Flutter Point Prediction

Computation of the LCO behavior via the HB/LCO solution methodology proceeds by first determining the flutter onset condition. As noted before, experimentally measured point condition MP77 corresponds to an LCO condition. However, the observed LCO amplitude is very small. Approximately $|\bar{\alpha}_1| = 0.18$ deg (Fig. 15 of Knipfer and Schewe[5]). As will be shown subsequently, based on the predicted LCO behavior using the HB/LCO method, for such a small amplitude the flow conditions at measured point MP77 are likely to be very near the flutter onset condition. For this analysis, we are considering this to be the case. As such, we are, in effect, assuming that the lift coefficient at the flutter onset condition is also $\bar{c}_{l_{0_f}} = 0.27$.

Rather than use a separate linearized unsteady aerodynamic solver to determine the flutter onset condition, one can instead simply run the HB CFD flow solver with a single harmonic ($N_H = 1$) and consider a very small-amplitude motion. As the amplitude of motion goes to zero, the HB solver yields exactly the same answer as a linearized unsteady solver. This is another useful feature of the HB solver.

Prediction of the linear flutter point condition, thus, consists of first tabulating linear unsteady aerodynamic loading data for plunge and pitch motions, respectively, for discrete reduced frequencies $\bar{\omega}$ over a range of reduced frequencies where flutter is presumed to occur. In this instance, we have chosen small unsteady motion amplitudes of $\bar{h}_1/b = 0.001$ and $\bar{\alpha}_1 = 0.001$ deg, respectively, for the plunge and pitch degrees of freedom, to simulate dynamically linear unsteady aerodynamics. Normalization of the calculated unsteady lift and moment coefficients by the respective amplitudes of either the plunge or the pitching motions, one then can obtain tabulated data for the unsteady aerodynamic transfer functions $\bar{c}_{l_{1_{\bar{h}_1/b}}}(\bar{\omega})$, $\bar{c}_{l_{1_{\bar{\alpha}_1}}}(\bar{\omega})$, $\bar{c}_{m_{1_{\bar{h}_1/b}}}(\bar{\omega})$, and $\bar{c}_{m_{1_{\bar{\alpha}_1}}}(\bar{\omega})$ at the preselected reduced frequencies $\bar{\omega}$. The 2×2 linear unsteady aerodynamic transfer function matrix $\boldsymbol{F}(\bar{\omega})$ is

$$\boldsymbol{F} = \begin{bmatrix} \bar{c}_{l_{1_{\bar{h}_1/b}}}(\bar{\omega}) & \bar{c}_{l_{1_{\bar{\alpha}_1}}}(\bar{\omega}) \\ \bar{c}_{m_{1_{\bar{h}_1/b}}}(\bar{\omega}) & \bar{c}_{m_{1_{\bar{\alpha}_1}}}(\bar{\omega}) \end{bmatrix} \tag{17}$$

and, for dynamically linear unsteady aerodynamics,

$$\boldsymbol{f} = \boldsymbol{F}\boldsymbol{u} \tag{18}$$

With the linear unsteady aerodynamic transfer functions tabulated for a range of real reduced frequencies, one can then use a "V–g" or similar type of method to solve for the flutter onset conditions. For example, by rewriting Eq. (2) as

$$[\boldsymbol{G} - (V^2/\pi)\boldsymbol{F}]\boldsymbol{u} = \boldsymbol{H}(V, \bar{\omega})\boldsymbol{u} = \boldsymbol{0} \tag{19}$$

one can search the plane of values for reduced velocity and reduced frequency $(V, \bar{\omega})$ for the condition(s) where the magnitude of the determinant of the 2×2 matrix $\boldsymbol{H}$ is a minimum. The use of this technique provides a quick and easy way to determine a good approximation of the flutter onset condition(s). This approximate flutter solution then provides a good starting solution for the HB/LCO method, which, when then run for a very small-amplitude motion, can be used to seek out the precise flutter onset condition. This is what has been done for the current flutter analysis of the NLR 7301 configuration. The results for the precise flutter onset conditions for the viscous and inviscid flow models are shown in Table 2, which also presents data for the LCO condition of experimental test point MP77.

Note from Table 2, that the computed flutter onset conditions are somewhat different than those observed for the MP77 test case. The numerical model predicts a lower flutter reduced velocity, and a higher flutter reduced frequency, respectively, for both the inviscid and viscous flow models. The MP77 experimental result for the structural eigenvector is also somewhat more plunge dominated than the computed values. Figure 15 of Knipfer and Schewe[5] was used to determine the value of $(\bar{h}_1/\bar{\alpha}_1 b)$ for the MP77 experimental condition. Note that Knipfer and Schewe[5] define the plunge coordinate has positive upward, opposite to our definition. We have corrected for this sign difference for the experimental value listed in Table 2.

We are currently trying to ascertain what possible causes might explain the differences between the experimental and computed conditions. Perhaps the steady flow CFD solution based on adjusting the angle-of-attack to match the experimental lift coefficient does not provide a sufficient approximation of the true wind-tunnel aerodynamic environment, or perhaps the MP77 test case corresponds to a flow condition more removed from the flutter onset condition.

We wish to also point out that we define mass ratio μ based on the wing model mass m, whereas Schewe and Deyhle,[3] Schewe et al.,[4] and Knipfer and Schewe[5] define the mass ratio based on the total plunge coordinate mass m_h. This, in turn, means that the reduced velocity is also defined somewhat differently. One may relate the two definitions for reduced velocity via $\sqrt{(m_h/m)}$. That is, our definition for reduced velocity is the product of the Schewe and Deyhle,[3] Schewe et al.,[4] and Knipfer and Schewe[5] definition multiplied by $\sqrt{(m_h/m)}$.

Table 1 Structural parameter values for the NLR 7301 aeroelastic configuration

Parameter	Value
Dimensional Quantities	
m	4.65 kg
m_{SD}	8.24 kg
m_{SP}	13.75 kg
I_α	$0.086\ \text{kg} \cdot \text{m}^2$
K_h	1.21×10^6 N/m
K_α	6.68×10^3 N · m/rad
S_α	$0.387\ \text{kg} \cdot \text{m}$
D_h	82.9 kg/s
D_α	$0.197\ \text{kg} \cdot \text{m}^2/(\text{s} \cdot \text{rad})$
ρ_∞	$0.383\ \text{kg/m}^3$
Nondimensional Quantities	
μ	172
x_α	0.555
r_α^2	0.822
ω_h/ω_α	1.83
ζ_h	0.0175
ζ_α	0.00411

Table 2 Computed flutter point conditions and NLR 7301 aeroelastic configuration experimental test case MP77 LCO conditions

Variable	Inviscid	Viscous	Experiment
$\bar{\alpha}_0$, deg	−1.55	0.20	——
$\bar{c}_{l_0}$	0.267	0.272	0.27
$\bar{c}_{m_0}$	−0.140	−0.0646	−0.082
V	0.371	0.385	0.488
$\bar{\omega}$	0.312	0.301	0.242
$\bar{\alpha}_1$, deg	0.0001	0.0001	0.18
$(\bar{h}_1/\bar{\alpha}_1 b)$	(1.15, 0.141)	(1.12, 0.172)	(1.66, 0)

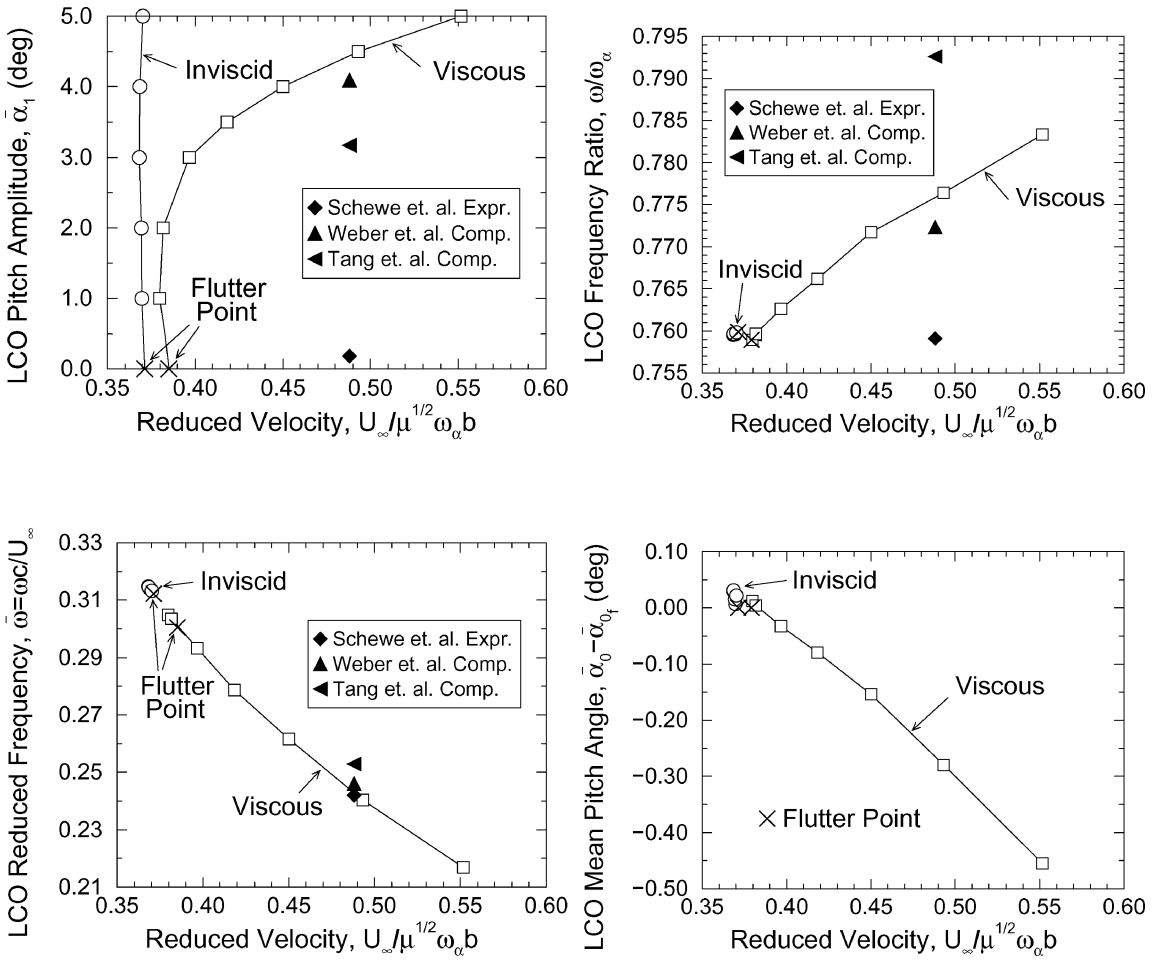

Fig. 9 LCO behavior trends for the NLR 7301 configuration: a) LCO amplitude, b) LCO frequency ratio, c) LCO reduced frequency, and d) LCO mean pitch angle.

Zero Spring Stiffness Angle of Attack

Next, the angle of attack corresponding to zero torsional spring stiffness α_{e_0} is computed for both the viscous and inviscid models. Once the flutter point is established, this value is easily determined by the use of Eq. (6). For the inviscid flow model, the value is $\alpha_{e_0} = -0.692$ (deg), and for the viscous flow model, the value is $\alpha_{e_0} = 0.645$ (deg).

Computed LCO Behavior

With the flutter onset condition established, along with a computed value for the angle of attack for zero torsional spring stiffness α_{e_0}, one can proceed with the LCO analysis for finite amplitude motions. Figure 9 shows computed LCO solution behavior trends for both the viscous and inviscid models of the NLR 7301 configuration. Also shown in Fig. 9 are the experimental LCO conditions as reported by Schewe and Deyhle,[3] Schewe et al.,[4] along with computed LCO conditions as determined by the investigations of Weber et al.[11] and Tang et al.[12] Clearly from the LCO amplitude vs reduced velocity curves shown in Fig. 9a, modeling viscous flow effects leads to a nonlinear soft or benign LCO behavior trend as discussed in the introduction, whereas the inviscid model exhibits a nearly linear aeroelastic LCO behavior trend. The flutter onset condition is also indicated in Fig. 9 and is less sensitive to viscous effects. Figures 9b and 9c show, respectively, LCO behavior trends for the frequency ratio and reduced frequency. The reduced frequency can be seen to change by a significant amount in the viscous case for large amplitudes. Finally, Fig. 9d shows the change in the LCO mean angle of attack $\bar{\alpha}_0$ with respect to reduced velocity. The LCO mean angle of attack is observed to decrease by approximately 0.5 deg from the flutter onset condition for the range of LCO amplitudes considered in the case of the viscous model. Because the aerodynamics are known to be extremely sensitive to small changes in the transonic region, it is likely to be important to model this effect.

Conclusions

An efficient procedure for computation of the LCO behavior of aeroelastic airfoil configurations in viscous transonic flows is presented. Viscous effects are demonstrated to be an important factor in the determination of the behavior of an LCO response with respect to reduced velocity. Viscous effects for the NLR 7301 aeroelastic configuration under investigation lead to a much more gradual rate of increase in LCO amplitude with respect to reduced velocity when compared to an inviscid model. The rapid increase in the computed LCO response beyond the flutter point emphasizes the importance of making careful and comprehensive experimental measurements of LCO response over a range of reduced velocities or other parameters as the flutter boundary is exceeded.

Acknowledgments

This work was supported by U.S. Air Force Office of Scientific Research (AFOSR) Grant, "Limit Cycle Oscillations and Nonlinear Aeroelastic Wing Response: Reduced Order Aerodynamics," and Small Business Technology Transfer Grant, "Nonlinear Reduced Order Modeling of Limit Cycle Oscillations of Aircraft Wings/Stores." The latter Grant is joint work with Zona Technology.

References

[1]Hall, K. C., Thomas, J. P., and Clark, W. S., "Computation of Unsteady Nonlinear Flows in Cascades Using a Harmonic Balance Technique," *AIAA Journal*, Vol. 40, No. 5, 2002, pp. 879–886.

[2]Thomas, J. P., Dowell, E. H., and Hall, K. C., "Nonlinear Inviscid Aerodynamic Effects on Transonic Divergence, Flutter, and Limit-Cycle Oscillations," *AIAA Journal*, Vol. 40, No. 4, 2002, pp. 638–646.

[3]Schewe, G., and Deyhle, H., "Experiments on Transonic Flutter of a Two-Dimensional Supercritical Wing with Emphasis on Non-Linear Effects," *Proceeding of the Royal Aeronautical Society Conference on Unsteady Aerodynamics*, Royal Aeronautical Society, London, July 1996.

[4]Schewe, G., Knipfer, A., Mai, H., and Dietz, G., "Experimental and Numerical Investigation of Nonlinear Effects in Transonic Flutter," English Version German Aerospace Center, DLR Final Rept. DLR IB 232–2002 J 01, Jan. 2002 (translated by W. F. King III, Gettingen, Germany).

[5]Knipfer, A., and Schewe, G., "Investigations of an Oscillating Supercritical 2D Wing Section in Transonic Flow," AIAA Paper 99-0653, Jan. 1999.

[6]McMullen, M., Jameson, A., and Alonso, J. J., "Acceleration of Convergence to Period Steady State in Turbomachinery Flows," AIAA Paper 2001-0152, Jan. 2001.

[7]McMullen, M., Jameson, A., and Alonso, J. J., "Application of a Non-Linear Frequency Domain Solver to the Euler and Navier-Stokes Equations," AIAA Paper 2002-0120, Jan. 2002.

[8]Ni, R., "A Multiple Grid Scheme for Solving the Euler Equations," *AIAA Journal*, Vol. 20, Nov. 1982, pp. 1565–1571.

[9]Saxor, A. P., "A Numerical Analysis of 3-D Inviscid Stator/Rotor Interactions Using Non-Reflecting Boundary Conditions," Gas Turbine Lab. Rept. 209, Massachusetts Inst. of Technology, Cambridge, MA, March 1992.

[10]Spalart, P. R., and Allmaras, S. R., "A One Equation Turbulence Model for Aerodynamic Flows," AIAA Paper 92-0439, Jan. 1992.

[11]Weber, S., Jones, K. D., Ekaterinaris, J. A., and Platzer, M. F., "Transonic Flutter Computations for a 2D Supercrtical Wing," AIAA Paper 99-0798, Jan. 1999.

[12]Tang, L., Bartels, R. E., Chen, P. C., and Liu, D. D., "Numerical Investigation of Transonic Limit Cycle Oscillations of a Two-Dimensional Supercritical Wing," *Journal of Fluids and Structures*, Vol. 17, No. 1, 2003, pp. 29–41.

[13]Castro, B. M., Jones, K. D., Ekaterinaris, J. A., and Platzer, M. F., "Analysis of the Effect of Porous Wall Interference on Transonic Airfoil Flutter," AIAA 2001-2725, June 2001.

[14]Castro, B. M., Ekaterinaris, J. A., and Platzer, M. F., "Navier–Stokes Analysis of Wind-Tunnel Interference on Transonic Airfoil Flutter," *AIAA Journal*, Vol. 40, No. 7, 2002, pp. 1269–1276.